Quantum percolation transition in three dimensions: Density of states, finite-size scaling, and multifractality

László Ujfalusi* and Imre Varga†

Elméleti Fizika Tanszék, Fizikai Intézet, Budapesti Műszaki és Gazdaságtudományi Egyetem, H-1521 Budapest, Hungary

(Received 9 May 2014; revised manuscript received 22 October 2014; published 18 November 2014)

The phase diagram of the metal-insulator transition in a three-dimensional quantum percolation problem is investigated numerically based on the multifractal analysis of the eigenstates. The large-scale numerical simulation has been performed on systems with linear sizes up to $L = 140$. The multifractal dimensions, exponents D_q and α_q, have been determined in the range of $0 \leqslant q \leqslant 1$. Our results confirm that this problem belongs to the same universality class as the three-dimensional Anderson model; the critical exponent of the localization length was found to be $\nu = 1.622 \pm 0.035$. However, the multifractal function $f(\alpha)$ and the exponents D_q and α_q produced anomalous variations along the phase boundary, $p_c^Q(E)$.

DOI: 10.1103/PhysRevB.90.174203 PACS number(s): 71.23.−k, 71.30.+h, 72.15.Rn

I. INTRODUCTION

The disorder-induced metal-insulator transition, which is a genuine quantum phase transition, has been one of the most studied phenomena of condensed-matter physics since the seminal paper published over five decades ago [1]. According to the original problem, the Hamiltonian

$$\mathcal{H} = \sum_i \varepsilon_i a_i^\dagger a_i - t \sum_{\langle i,j \rangle} (a_i^\dagger a_j + a_j^\dagger a_i) \tag{1}$$

describes the behavior of noninteracting spinless electrons in disorder. The first term in Eq. (1) represents an on-site disordered potential, where the energies, ε_i, are independent, uncorrelated random variables, drawn from a distribution function, $P(\varepsilon)$, whose form is usually chosen to be uniform over an energy range that is symmetric around $\varepsilon = 0$, but other forms, e.g., Gaussian or binary distributions, could be used as well. The second term in Eq. (1) is the kinetic energy describing the hopping of the particles over a regular lattice, but restricted to nearest neighbors only. The energy scale associated with the hopping process, t, can be taken as the unit of energy ($t = 1$). The sites form a regular, usually simple cubic lattice. The embedding dimension, d, of the system is a very important parameter, since phase transition occurs for $d > 2$ only [2].

Besides diagonal disorder resembling substitutional disorder, the other main cause of irregularity in condensed systems is structural disorder. For the investigation of topological and structural disorder, percolation is one of the most important and widely used models. Percolation in general has wide applicability in many fields of physics [3]. In the Bernoulli site-percolation problem, every site is filled with probability p and is empty with probability $1 - p$ independently. The main goal of classical percolation is to tell for a given p whether an infinite cluster of filled sites may exist in the thermodynamic limit or not. It turns out that there is such a critical probability, p_c^c, below which ($p < p_c^c$) there is no infinite cluster, but above which ($p > p_c^c$) there is. In one dimension [4], $p_c^c = 1$; in two dimensions [5], $p_c^c = 0.592\,746\,216 \pm 0.000\,000\,13$; in three dimensions [3], $p_c^c = 0.3116 \pm 0.0002$. In the $p > p_c^c$ case, the existence of an infinite cluster ensures that the system can be treated as a conductor, since classical particles can travel through the whole system. On the other hand, if $p < p_c^c$, the system consists of a set of disjoint, finite clusters, and as a consequence it behaves as an insulator, since no particle can escape from its initial finite cluster.

For the electric conduction properties of a sample, the electrons are responsible whose behavior is described very well by quantum mechanics, therefore we shall investigate spinless noninteracting electrons on a percolated lattice; this is called the quantum percolation model. Omitting spin and interaction is necessary because even with these simplifications, the problem seems to be hard to solve. The corresponding Hamiltonian is

$$\mathcal{H} = \sum_{i \in A} \varepsilon a_i^\dagger a_i - \sum_{\substack{\langle i,j \rangle \\ i,j \in A}} (a_i^\dagger a_j + a_j^\dagger a_i), \tag{2}$$

where A is the set of filled sites, and ε is a constant on-site energy, whose value can be safely set to zero without loss of generality. Note that the pure site-percolation problem is equivalent to a binary Anderson model [7–9] with constant ε_A and ε_B but taking the limit $\varepsilon_B \to \infty$:

$$\mathcal{H} = \sum_{i \in A} \varepsilon_A a_i^\dagger a_i + \sum_{i \in B} \varepsilon_B a_i^\dagger a_i - \sum_{\langle i,j \rangle} (a_i^\dagger a_j + a_j^\dagger a_i). \tag{3}$$

This Hamiltonian could describe an alloy of a perfect metal consisting of atoms A and a perfect insulator consisting of atoms B only. All A sites are equivalent, and the B sites cannot be reached due to their infinite on-site energy, therefore B sites behave as if they were empty. This suggests that quantum percolation behaves similar to the Anderson model. In our present work, we shall show many similarities. The most important similarity with the Anderson problem is the existence of a metal-insulator transition for the quantum percolation model too, however here p, or strictly speaking $(1 - p)$, plays the role of disorder: For $p < p_c^c$, every state is localized onto finite, connected islands, thus the sample is an insulator. Increasing p beyond p_c^c, however, a classical particle can travel through the sample, the electron wave functions are localized due to strong interference effects caused by disorder, and the sample still remains an insulator. For p values slightly

*ujfalusi@phy.bme.hu
†varga@phy.bme.hu

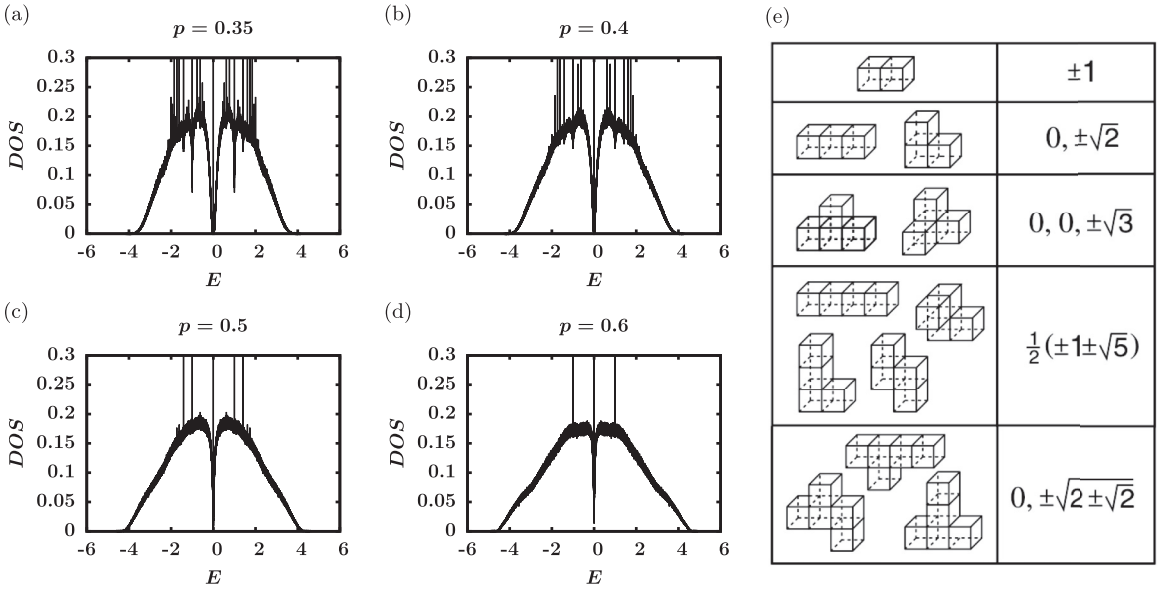

FIG. 1. Left side: Density of states of the quantum percolation model at different site-filling probabilities: (a) $p = 0.35$, (b) $p = 0.4$, (c) $p = 0.5$, and (d) $p = 0.6$. (e) Small clusters corresponding to special energies taken from the review of Schubert and Fehske [6].

below 1, states are perturbed Bloch states, and the sample is a metal. In between, there exists a mobility edge, $p_c^Q(E)$, that is an energy-dependent quantum critical point, below which electronic eigenstates are Anderson-localized giving rise to an insulator, and above which they are extended forming a metal. Along the mobility edge, $p_c^Q(E)$, the states are supposed to be multifractals. In Sec. III B, we argue that the Anderson model and the quantum percolation model belong to the same universality class.

The organization of the paper is the following. In Sec. II we examine the peculiar properties of the density of states in quantum percolation, and we provide an overview about multifractality together with an introduction about the finite-size scaling analysis of the corresponding generalized dimensions. In Sec. III A we give a short overview of the technique of the latter analysis in the case of the three-dimensional (3D) Anderson transition, in Sec. III B we present the methods applied in the present work, and in Sec. IV we give the results of our analysis for the multifractal analysis. Finally, Sec. V is left for a summary.

II. THEORETICAL AND NUMERICAL BACKGROUND

Electronic conduction is only possible on an infinite cluster, so $p_c^Q > p_c^C$ is expected; therefore, the infinite cluster should be investigated, so only the $p > p_c^C$ regime is interesting for us. Since numerically we can deal with a finite lattice only, we restricted our work to the largest finite cluster found by a Hoshen-Kopelman algorithm [10]. In a finite-size sample, the Hamiltonian Eq. (2) is a huge sparse matrix. To obtain the spectrum and eigenfunctions, we used the Jacobi-Davidson method encoded in the PRIMME package [11] with ILU preconditioning using the ILUPACK package [12].

We will first examine the density of states (DOS), because for the quantum percolation problem it deserves a special attention.

A. Density of states

The DOS of the giant cluster has an unusual form. The evolution of this function with p is depicted in Fig. 1. With increasing disorder, which in the present case means decreasing p, more and more sharp peaks appear in the spectrum. These peaks correspond to special so-called "molecular states," which are localized to a few sites [7]. These states are nonzero on a few sites only and exactly zero on every other one due to exact destructive interference. Therefore, they are not localized in the sense of Anderson localization, because there is no exponential decay in the wave-function envelope. Typical few-site structures and corresponding energies are given on the right side of Fig. 1. Since the value $E = 0$ appears for most clusters as an eigenvalue, the highest peak of the DOS is at the middle of the band, and there is also a pseudogap around it.

Considering other few-site clusters, there is no reason for the eigenvalues to avoid any part of the band, therefore peaks in the DOS corresponding to molecular states should appear densely in the thermodynamic limit. The energy of a molecular state is a strict value, thus the peaks in the DOS appear as a series of Dirac δs. As we can see, the spectrum consists of two parts: a dense point spectrum due to molecular states, and a continuous one due to all other states [7]. This statement has been rigorously proven recently in the case of a two-dimensional (2D) square lattice, and for tree graphs corresponding to an effective infinite dimension, therefore it is conjectured to be true in any dimension [13].

Since molecular states are strongly localized, they cannot contribute to conduction. Therefore, we restrict our investigation to the continuous part of the spectrum only. With the numerical method described above, we are able to compute one single eigenstate of the Hamiltonian having an eigenenergy close to a given value of E. In Fig. 1 it is shown that in a finite system, molecular states appear frequently at a few special energies only, e.g., $E = 0, \pm 1, \pm\sqrt{2}, \ldots$, therefore for our

purpose we have chosen energy windows avoiding the peaks in the DOS.

The cubic lattice is a bipartite lattice, and the Hamiltonian (2) couples nearest neighbors only, therefore from one sublattice, α, it is possible to hop to the other sublattice, β, only. The Hamiltonian anticommutes with an operator C, which is 1 on sublattice α and -1 on sublattice β, thus C acts like a chirality transformation [14]. Therefore, the quantum percolation model is symmetric not only on average for the exchange of eigenenergies, $-E \leftrightarrow E$, but for every single disorder realization. In the low- (high-) energy range, the states have antibonding (bonding) character. In the middle of the band, around $E = 0$, chessboard-like chiral states appear. These chiral states exactly at $E = 0$ are eigenfunctions of C as well, therefore they are protected against off-diagonal disorder.

To understand the subgap appearing around the middle of the band, $E = 0$, we invoke the arguments of Ref. [14]. The square of the Hamiltonian, $\mathcal{H}^2$, connects the sites of the same sublattice only, see Fig. 2, thus one can "renormalize" $\mathcal{H}^2$ acting on one of the sublattices [14]. The vicinity of $E = 0$ belongs to the low-energy regime of the spectrum of $\mathcal{H}^2$, therefore here antibonding states should appear, which are more or less visible in the wave functions themselves, too. But the hopping elements to the diagonal-lying second neighbors in Fig. 2 introduce triangles. Triangles and the antibonding nature together lead to frustration. Based on the frustration of the states around zero energy, Naumis *et al.* [14] showed in two dimensions that the width of the pseudogap around zero energy, Δ, is connected to the peak at $E = 0$: $\Delta \sim \sqrt{\rho_0}$, where ρ_0 stands for the weight of the zero-energy states in the spectra. They also showed that the width of the pseudogap tends to zero in the nondisordered limit, $\lim_{p\to 1} \Delta = 0$. The extension of these arguments to three dimensions should be valid, since the most important ingredient of their calculation is the coordination number of the lattice and not the dimensionality itself explicitly.

The states close to $E = 0$ belong to the edge of the spectrum of $\mathcal{H}^2$, which is a disordered Hamiltonian. Therefore, the pseudogap might be qualitatively interpreted as the Lifshitz tail of $\mathcal{H}^2$, leading to localized states close $E = 0$.

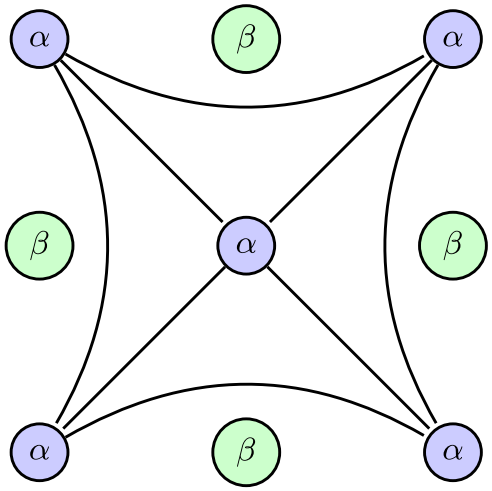

FIG. 2. (Color online) Hopping elements in the "renormalized" Hamiltonian, $\mathcal{H}^2$.

B. Introduction to multifractals

In recent high-precision calculations [15], the so-called multifractal exponents (MFEs) have been used to describe the Anderson metal-insulator transition (AMIT). The renormalization flow of the AMIT as mentioned in the Introduction has three fixed points: a metallic, an insulating, and a critical one. In the metallic fixed point, every state is extended with probability 1, thus with increasing system size the effective size of the states also grows proportional to the volume. So the fractal dimension of the states, which will be defined more precisely later, is just the embedding dimension q-independently, $D_q^{\text{met}} \equiv d$. In the insulating fixed point, every state is exponentially localized; their effective size does not change with growing system size, thus for $q \geqslant 0$, $D_q^{\text{ins}} \equiv 0$, and for $q < 0$, $D_q^{\text{ins}} \equiv \infty$. At criticality, the system does not change during renormalization, thus it must be statistically the same on all length scales showing scale independence, which means self-similarity. Therefore, wave functions are multifractals, in other words generalized fractals [16]; see Fig. 3.

In our case, there is a d-dimensional hypercubic lattice with linear size L, and a normalized wave function whose support is this lattice, $\sum_{i=1}^{L^d} |\Psi_i|^2 = 1$, defining a probability distribution. Let us divide this lattice into smaller hypercubes (boxes) with linear size ℓ, and introduce the ratio $\lambda = \frac{\ell}{L}$. Then coarse graining $|\psi|^2$, in other words summing all its values in the kth box, we obtain

$$\mu_k = \sum_{i \in \text{box}_k} |\Psi_i|^2, \tag{4}$$

where μ_k is the weight associated with the kth box, termed the box probability. Let us define the qth moment of the mass, frequently called the generalized inverse participation ratio (GIPR), and its derivative as

$$R_q = \sum_{k=1}^{\lambda^{-d}} \mu_k^q = \lambda^{\tilde{\tau}_q}, \quad S_q = \frac{dR_q}{dq} = \sum_{k=1}^{\lambda^{-d}} \mu_k^q \ln \mu_k, \tag{5}$$

where $\tilde{\tau}_q$ is the finite system mass exponent. $\tilde{\tau}_q$ and its derivative read

$$\tilde{\tau}_q = \frac{\ln R_q}{\ln \lambda}, \quad \tilde{\alpha}_q = \frac{d\tilde{\tau}_q}{dq} = \frac{S_q}{R_q \ln \lambda}. \tag{6}$$

Taking the $L \to \infty$ limit, which is equivalent to taking the $\lambda \to 0$ limit, the mass exponent and its derivative are

$$\tau_q = \lim_{\lambda\to 0} \frac{\ln R_q}{\ln \lambda}, \quad \alpha_q = \frac{d\tau_q}{dq} = \lim_{\lambda\to 0} \frac{S_q}{R_q \ln \lambda}. \tag{7}$$

τ_q can be written in the form

$$\tau_q = D_q(q-1) = d(q-1) + \Delta_q, \tag{8}$$

where D_q is the generalized fractal dimension. In this expression, Δ_q is the anomalous scaling exponent:

$$D_q = \frac{1}{q-1} \lim_{\lambda\to 0} \frac{\ln R_q}{\ln \lambda}, \quad \Delta_q = (D_q - d)(q-1). \tag{9}$$

The quantities τ_q, α_q, D_q, and Δ_q are often referred to as MFEs, while the finite system version of these exponents, $\tilde{\tau}_q$, $\tilde{\alpha}_q$, $\tilde{D}_q$, and $\tilde{\Delta}_q$, are called generalized multifractal exponents (GMFEs). D_q is directly related to the so-called *Rényi*

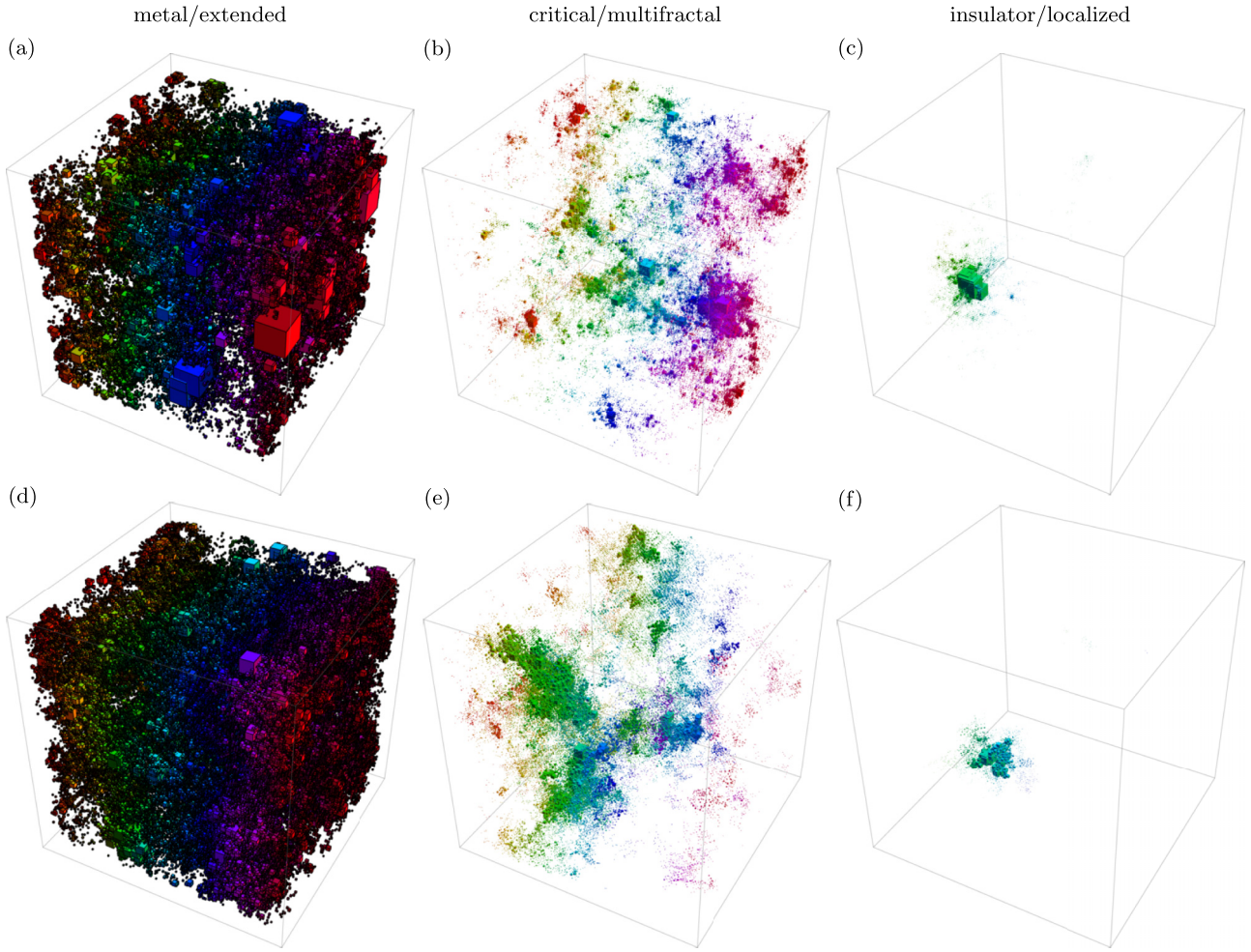

FIG. 3. (Color online) First row: Eigenvectors of the Anderson model at $E = 0$ (a) on the metallic side at $W = 14$, (b) close to criticality $W = 16.5$, and (c) on the insulating side at $W = 20$. Second row: eigenvectors of the quantum percolation model at energy $E = 0.1$, (d) on the metallic side at $p = 0.5$, (e) close to criticality, $p = 0.4535$, and (f) on the insulating side at $p = 0.4$. Box sizes correspond to (a),(d) $400 \times \sqrt{|\Psi|^2}$; (b),(e) $70 \times \sqrt{|\Psi|^2}$; and (c),(f) $20 \times \sqrt{|\Psi|^2}$. Multiplying factors were tuned to best sight but without overlapping cubes. System size, $L = 120$, for all subfigures. Coloring is due to the x coordinate.

entropy, $H_q = (q-1)^{-1} \ln R_q$, which in the limit $q \to 1$ yields the well-known *Shannon entropy*, i.e., $-\sum_k \mu_k \ln \mu_k$. This is the reason why D_1 is also referred to as information dimension:

$$D_1 = \lim_{q\to 1} \frac{1}{q-1} \lim_{\lambda\to 0} \frac{\ln R_q}{\ln \lambda}$$

$$\stackrel{L'H}{=} \alpha_1 = \lim_{\lambda\to 0} \frac{1}{\ln \lambda} \sum_{k=1}^{\lambda^{-d}} \mu_k \ln \mu_k, \tag{10}$$

while another frequently used dimension is the correlation dimension, D_2. The latter dimension appeared often in recent studies of the physical relevance of multifractal eigenstates [17].

There is another way to characterize the multifractal nature of the wave functions. For that purpose, the box probability μ can be transformed into another variable, $\alpha = \ln \mu / \ln \lambda$, assuming the fractal scaling

$$\mu \sim \lambda^{\alpha}. \tag{11}$$

Let us denote the probability density function of the number of boxes having a value α with $\mathcal{P}(\alpha)$. The scaling of $\mathcal{P}(\alpha)$ is described through the singularity spectrum $f(\alpha)$, which is the fractal dimension of the number of boxes having a value α:

$$\mathcal{P}(\alpha) \sim \lambda^{f(\alpha)}. \tag{12}$$

Function $f(\alpha)$ is merely the Legendre transform of τ_q:

$$f(\alpha_q) = q\alpha_q - \tau_q. \tag{13}$$

According to recent results, a symmetry relation exists for α_q and Δ_q given in the form [18]

$$\Delta_q - \Delta_{1-q} = 0, \qquad \alpha_q + \alpha_{1-q} = 2d. \tag{14}$$

This relation was first obtained for some random matrix ensemble numerically, and using the supersymmetric nonlinear sigma model analytically [18] it was later confirmed for several two-dimensional [19,20] and three-dimensional systems [21]. However, deviations have been detected in other cases [23,24]. The robustness of this relation has been investigated also for many-body localization [25].

C. Finite-size scaling laws for GMFEs

Finite-size scaling techniques are very well described by Rodriguez *et al.* [15] for the Anderson model. We are going to use their notation, therefore we denote disorder by W. In this subsection, we extend the formalism of Ref. [15]. From the eigenfunction, the R_q and S_q values can be computed for every state at different q values. At fixed disorder, W, system size, L, and box size, ℓ, every GMFE is computable from these two quantities in the following way [15]:

$$\tilde{\tau}_q^{\rm ens}(W,L,\ell) = \frac{\ln\langle R_q\rangle}{\ln\lambda}, \quad \tilde{\tau}_q^{\rm typ}(W,L,\ell) = \frac{\langle \ln R_q\rangle}{\ln\lambda}, \tag{15a}$$

$$\tilde{\alpha}_q^{\rm ens}(W,L,\ell) = \frac{\langle S_q\rangle}{\langle R_q\rangle \ln\lambda}, \tag{15b}$$

$$\tilde{\alpha}_q^{\rm typ}(W,L,\ell) = \left\langle \frac{S_q}{R_q}\right\rangle \frac{1}{\ln\lambda}, \tag{15b}$$

$$\tilde{D}_q^{\rm ens}(W,L,\ell) = \frac{1}{q-1}\frac{\ln\langle R_q\rangle}{\ln\lambda}, \tag{15c}$$

$$\tilde{D}_q^{\rm typ}(W,L,\ell) = \frac{1}{q-1}\frac{\langle \ln R_q\rangle}{\ln\lambda}, \tag{15c}$$

$$\tilde{\Delta}_q^{\rm ens}(W,L,\ell) = \frac{\ln\langle R_q\rangle}{\ln\lambda} - d(q-1), \tag{15d}$$

$$\tilde{\Delta}_q^{\rm typ}(W,L,\ell) = \frac{\langle \ln R_q\rangle}{\ln\lambda} - d(q-1), \tag{15d}$$

where $\langle\,\rangle$ stands for averaging: "ens" and "typ" denote the ensemble and typical averaging. Every GMFE approaches the value of the corresponding MFE at the critical point only in the limit $\lambda \to 0$. Close to the critical point due to standard finite-size scaling arguments, we can suppose that R_q and S_q show scaling behavior determined only by the ratio of two length scales, L and ℓ, and the localization/correlation length, ξ, in the insulating/metallic phase:

$$R_q(W,L,\ell) = \lambda^{\tau_q}\mathcal{R}_q\left(\frac{L}{\xi},\frac{\ell}{\xi}\right). \tag{16}$$

According to (15a)–(15d), for all GMFEs the scaling-law holds independently of the type of averaging [15]:

$$\tilde{\tau}_q(W,L,\ell) = \tau_q + \frac{q(q-1)}{\ln\lambda}\mathcal{T}_q\left(\frac{L}{\xi},\frac{\ell}{\xi}\right), \tag{17a}$$

$$\tilde{\alpha}_q(W,L,\ell) = \alpha_q + \frac{1}{\ln\lambda}\mathcal{A}_q\left(\frac{L}{\xi},\frac{\ell}{\xi}\right), \tag{17b}$$

$$\tilde{D}_q(W,L,\ell) = D_q + \frac{q}{\ln\lambda}\mathcal{T}_q\left(\frac{L}{\xi},\frac{\ell}{\xi}\right), \tag{17c}$$

$$\tilde{\Delta}_q(W,L,\ell) = \Delta_q + \frac{q(q-1)}{\ln\lambda}\mathcal{T}_q\left(\frac{L}{\xi},\frac{\ell}{\xi}\right). \tag{17d}$$

Equations (17a)–(17d) can be summarized in one equation:

$$\tilde{G}_q(W,L,\ell) = G_q + \frac{1}{\ln\lambda}\mathcal{G}_q\left(\frac{L}{\xi},\frac{\ell}{\xi}\right). \tag{18}$$

(L,ℓ) on the left and $(\frac{L}{\xi},\frac{\ell}{\xi})$ on the right can be changed to (L,λ) and $(\frac{L}{\xi},\lambda)$:

$$\tilde{G}_q(W,L,\lambda) = G_q + \frac{1}{\ln\lambda}\mathcal{G}_q\left(\frac{L}{\xi},\lambda\right). \tag{19}$$

1. Finite-size scaling at fixed λ

At fixed λ, G_q in Eq. (19) can be considered as the constant term of $\mathcal{G}_q$, therefore

$$\tilde{G}_q(W,L) = \mathcal{G}_q\left(\frac{L}{\xi}\right), \tag{20}$$

where the constant λ has been dropped. $\mathcal{G}_q$ can be expanded with one relevant, $\varrho(w)$, and one irrelevant operator, $\eta(w)$, in the following way using $w = W - W_c$:

$$\mathcal{G}_q(\varrho L^{\frac{1}{\nu}},\eta L^{-y}) = \mathcal{G}_q^{\rm rel}(\varrho L^{\frac{1}{\nu}}) + \eta L^{-y}\mathcal{G}_q^{\rm irrel}(\varrho L^{\frac{1}{\nu}}). \tag{21}$$

All the disorder-dependent quantities in the above formula can be expanded in Taylor series:

$$\mathcal{G}_q^{\rm rel}(\varrho L^{\frac{1}{\nu}}) = \sum_{i=0}^{n_{\rm rel}} a_i(\varrho L^{\frac{1}{\nu}})^i, \tag{22}$$

$$\mathcal{G}_q^{\rm irrel}(\varrho L^{\frac{1}{\nu}}) = \sum_{i=0}^{n_{\rm irrel}} b_i(\varrho L^{\frac{1}{\nu}})^i, \tag{23}$$

$$\varrho(w) = w + \sum_{i=2}^{n_\varrho} c_i w^i, \quad \eta(w) = 1 + \sum_{i=1}^{n_\eta} d_i w^i. \tag{24}$$

The number of parameters is $n_{\rm rel} + n_{\rm irrel} + n_\rho + n_\eta + 1$.

2. Finite-size scaling at fixed ℓ = 1

For fixed ℓ, the scaling law given in Eq. (18) has to be considered. The expansion of $\mathcal{G}$ in (18) is

$$\begin{aligned}\mathcal{G}_q(\varrho L^{\frac{1}{\nu}},\varrho\ell^{\frac{1}{\nu}},\eta L^{-y},\eta'\ell^{-y'}) &= \mathcal{G}_q^{\rm rel}(\varrho L^{\frac{1}{\nu}},\varrho\ell^{\frac{1}{\nu}}) + \eta L^{-y}\mathcal{G}_q^{\rm irrel}(\varrho L^{\frac{1}{\nu}},\varrho\ell^{\frac{1}{\nu}}) \\ &\quad + \eta'\ell^{-y'}\mathcal{G}_q'^{\rm irrel}(\varrho L^{\frac{1}{\nu}},\varrho\ell^{\frac{1}{\nu}}).\end{aligned}$$

Choosing $\ell = 1$, and considering that in most cases η and η' are constant, i.e., $n_\eta = 0$, the last term can be merged with the relevant part. Equation (18) has the following form for fixed $\ell = 1$:

$$\tilde{G}_q(W,L) = G_q + \frac{1}{\ln L}\left[\mathcal{G}_q^{\rm rel}(\varrho L^{\frac{1}{\nu}},\varrho) + \eta L^{-y}\mathcal{G}_q^{\rm irrel}(\varrho L^{\frac{1}{\nu}},\varrho)\right]. \tag{25}$$

The Taylor expansions of the above functions are

$$\mathcal{G}_q^{\rm rel}(\varrho L^{\frac{1}{\nu}},\varrho) = \sum_{i=0}^{n_{\rm rel}}\sum_{j=0}^{i} a_{ij}\varrho^i L^{\frac{j}{\nu}}, \tag{26}$$

$$\mathcal{G}_q^{\rm irrel}(\varrho L^{\frac{1}{\nu}},\varrho) = \sum_{i=0}^{n_{\rm rel}}\sum_{j=0}^{i} b_{ij}\varrho^i L^{\frac{j}{\nu}}, \tag{27}$$

$$\varrho_{(w)} = w + \sum_{i=2}^{n_\varrho} c_i w^i, \quad \eta_{(w)} = 1 + \sum_{i=1}^{n_\eta} d_i w^i. \tag{28}$$

The number of parameters is $3n_{\rm rel}(n_{\rm rel}+1)/2+3n_{\rm irrel}(n_{\rm irrel}+1)/2+n_\rho+n_\eta-1$. We can see that the number of parameters grows as $\sim n^2_{\rm rel/irrel}$ for fixed $\ell=1$, instead of $\sim n_{\rm rel/irrel}$ as for fixed λ. This makes the fitting procedure definitely much more difficult.

III. FINITE-SIZE SCALING FOR THE 3D QUANTUM PERCOLATION MODEL USING GMFEs

Before turning to the analysis of our simulations on the 3D quantum percolation model, we briefly review the details of the finite-size scaling using GMFEs but first based on the 3D Anderson model. The aim of this section is twofold. First of all, we present the advantages and disadvantages of the various methods used and their applicability for our purposes. Second, we show the precision of these techniques for the case of a well-studied case, namely the Anderson transition.

A. Finite-size scaling for the 3D Anderson model using GMFEs

Our first goal was to test our numerical algorithm on the well-known Anderson problem. Based on Ref. [15], we formulate two cases: first fixing λ and then fixing ℓ.

1. Finite-size scaling at fixed λ

Since the metal-insulator transition occurs at the band center [2] ($E=0$) at disorder, $W_c\approx 16.5$, most works study the vicinity of this point. To have the best comparison, we analyzed this regime also, therefore about 20 disorder values were taken for the range $15\leqslant W\leqslant 18$. System sizes were taken from the range $L=20$–100, and the number of samples was $N=4000$ at least. We considered only one wave function per realization, the one with energy closest to zero in order to avoid correlations between wave functions of the same system [15]. From the wave function, the R_q and S_q multifractal moments were calculated in the range $-1\leqslant q\leqslant 2$ at fixed $\lambda=0.1$. In Eqs. (17a)–(17d), only two scaling functions are present, $\mathcal{T}_q$ and $\mathcal{A}_q$, therefore we investigated $\tilde{D}_q(W,L,\lambda=0.1)$ and $\tilde{\alpha}_q(W,L,\lambda=0.1)$ only using ensemble and typical averaging (see Sec. II C).

To fit the scaling law (20), we used MINUIT. To find the best fit to the data obtained numerically, the order of expansion of $\mathcal{G}_q^{\rm rel/irrel}$, ϱ, and η must be decided by choosing the values of $n_{\rm rel}$,$n_{\rm irrel}$,n_ϱ, and n_η. Since the relevant operator is more important than the irrelevant one, we always used $n_{\rm rel}\geqslant n_{\rm irrel}$ and $n_\varrho\geqslant n_\eta$. To choose the order of the expansion, we used basically three criteria. The first criterion we took into account was how close the ratio $\chi^2/({\rm NDF}-1)$ approached 1. χ^2 is the sum of the squared differences between the data points and the best fit weighted by the inverse variance of the data points, and NDF is the number of degrees of freedom, namely the number of data points minus the number of fit parameters. A ratio $\chi^2/({\rm NDF}-1)\approx 1$ means that the deviations from the best fit are in the order of the standard deviation. The second criterion was that the fit has to be stable against changing the expansion orders, i.e., adding a few new expansion terms. From the fits that fulfilled the first two criteria, we chose the simplest model with the lowest expansion orders. Sometimes we also took into account the error bars, and we chose the model with the lowest error bar for the most important quantities (W_c,ν, etc.) if similar models fulfilled the first two criteria.

The error bars of the best-fit parameters were obtained by a Monte Carlo simulation. The data points are results of averaging, so due to the central limit theorem, they have a Gaussian distribution. Therefore, we generated Gaussian random numbers with parameters corresponding to the mean and standard deviation of the raw data points, and then we found the best fit. Repeating this procedure $N_{\rm MC}=100$ times provided us with the distribution of the fit parameters. We chose a 95% confidence level to obtain the error bars. We performed FSS for $\tilde{D}_q^{\rm ens}$,$\tilde{D}_q^{\rm typ}$,$\tilde{\alpha}_q^{\rm ens}$, and $\tilde{\alpha}_q^{\rm typ}$.

The results were very similar to the ones obtained by Rodriguez *et al.* [15]. In the investigated range of q the results were q-independent for $\tilde{D}_q^{\rm ens}$,$\tilde{D}_q^{\rm typ}$,$\tilde{\alpha}_q^{\rm ens}$, and $\tilde{\alpha}_q^{\rm typ}$ within a 95% confidence interval. The numerical values of W_c, ν, and y have been obtained in excellent agreement with the results of Ref. [15]. Hence we concluded that our method has been confirmed. The disadvantage of this method is that the constant term of $\mathcal{G}_q$ is not equal to the corresponding MFE, since λ is fixed instead of tending to zero. It would be possible to perform multifractal finite-size scaling (MFSS) at different λs, and then obtain the MFEs for $\lambda\to 0$.

2. Finite-size scaling at fixed ℓ

The main goal of the present work is to investigate the quantum percolation problem, where a fraction of lattice points is missing. In this case, when performing the coarse-graining technique defined above, immediate difficulties arise. It is not clear how the ℓ-sized boxes have to be made, or how the boxes containing different numbers of filled sites should be compared. One way to resolve this problem is to choose $\ell=1$, meaning that a box contains only one site. Even though this choice eventually opens the possibility to extend the MFSS method for irregular lattices or even for graphs and networks in the future, there is also a huge price to be paid: the smoothing effect of the coarse graining is lost, and only the more complicated method of the fixed-ℓ technique described in Sec. II C 2 remains.

There is always some numerical noise on the data, which becomes even more relevant for the smallest wave-function components. In the case of negative q, these uncertain small values are dominating the sums in R_q and S_q [see Eqs. (5)]. Coarse graining clearly suppresses this effect, because for $\ell>1$ in an $\ell\times\ell\times\ell$ sized box, positive and negative errors can cancel each other. Another effect is that in a box large and small wave-function amplitudes appear together with high probability. In this way, the relative error of a μ_k box probability is reduced with coarse graining, in other words coarse graining has a nice smoothing effect. At fixed $\ell=1$ this effect is missing, thus for $q<0$ the numerically obtained $\tilde{D}_q^{\rm ens}$,$\tilde{D}_q^{\rm typ}$,$\tilde{\alpha}_q^{\rm ens}$, and $\tilde{\alpha}_q^{\rm typ}$ [see, e.g., Eqs. (15a)–(15d)] values are very noisy. This makes every attempt to get results for negative q very hard if not impossible.

The other problem is that the scaling law becomes more complicated as the leading number of fit parameters is growing as $\sim n^2_{\rm rel/irrel}$ for fixed $\ell=1$ instead of $\sim n_{\rm rel/irrel}$ as for fixed λ.

Performing the MFSS, another problem appeared with Eq. (25). During the fit, the irrelevant exponent, y, converged to

very small (10^{-3}–10^{-5}) or very large (10^{2}–10^{3}) values. In the first case, the irrelevant term can be merged with the relevant one, since η is in most cases constant. In the second case, L^{-y} suppresses the irrelevant part. This caused really large errors in the b_{ij}, and it rendered the whole irrelevant part meaningless.

To find out whether this is just a numerical problem or if there is also some systematic physical reason behind this behavior, we modeled the above problem: First a dataset was made by evaluating the expression (25) at system sizes and disorder we used before, with some expansion parameter values similar to the ones provided by previous MFSS procedures. Of course fitting Eq. (25) to this dataset gave a perfect fit. Now adding some small random noise to the initial dataset started to shift the resulting fit parameters a little. By increasing the noise to the order of the standard deviation of the original dataset for the Anderson model, the fit showed the expected phenomenon: The irrelevant exponent, y, converged to either large or small values. This shows that this is just a numerical artifact. There is a shift on the $\tilde{D}_q(W,L)$ curves for different system sizes; see Fig. 4. This shift comes mainly from the $1/\ln L$ term in Eq. (25), and if noise is present it is numerically hard to determine the effect of the L^{-y} irrelevant part. All in all, however, in a finite system irrelevant operators are always present, but considering them would only increase the error of the fit parameters. Therefore, it seems to be useful to drop the irrelevant part and to keep only the relevant one. In this way, the fitting function reads

$$\tilde{G}_q(W,L) = G_q + \frac{1}{\ln L}\left(\sum_{i=0}^{n_{\rm rel}}\sum_{j=0}^{i} a_{ij}\varrho^i L^{\frac{j}{\nu}}\right). \qquad (29)$$

We performed MFSS in the range $0 \leqslant q \leqslant 2$ with this formula at fixed $\ell = 1$ for the Anderson model. Similarly to the case of fixed λ at fixed energy E and q, one has to decide the order of the Taylor expansion of the $\mathcal{G}$ scaling function. To do this, we used similar criteria to those used before. The only difference was that unfortunately the fits were not as stable against changing the expansion orders, $n_{\rm rel}$ and n_ρ, as the ones for fixed λ, because at fixed $\ell = 1$ we had to fit many more parameters to the same amount of data. The value of the critical point must be q-independent, which—contrary to the case of fixed λ—we had to keep also as a criterion. We had to compare fits at different q values and choose the lowest expansion orders that led to a q-independent critical point, and

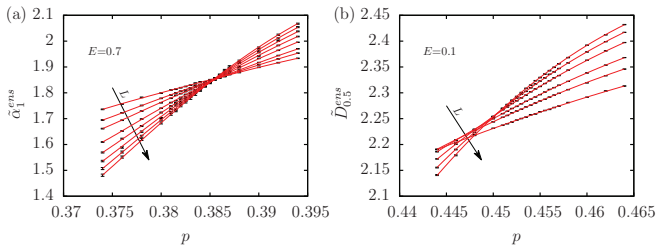

FIG. 4. (Color online) The generalized multifractal exponents (a) $\tilde{\alpha}_1^{\rm ens}(p,L,\ell=1)$ at $E=0.7$ and (b) $\tilde{D}_{0.5}^{\rm ens}(p,L,\ell=1)$ at $E=0.1$ for the 3D quantum percolation model. Points with error bars are the raw data, and red solid lines are the best fits of the function Eq. (29) as a function of disorder, p, at different system sizes, L.

we still had a $\chi^2/({\rm NDF}-1)$ ratio close to 1. In some cases, we also had to leave out the smallest system size(s), i.e., choose $L_{\rm min} = 30$ or 40 instead of 20 to fulfill the criteria above.

The results were acceptable only approximately in the range $0 \leqslant q \leqslant 1$. If $q \geqslant 1$, fit parameters started to shift, sometimes out of the confidence band of those obtained for smaller q values, and error bars were growing extremely large. Similar effects of growing error bars for $q \geqslant 1$ have been seen earlier on a moderate level at fixed $\lambda = 0.1$, where the help of the smoothing effect of coarse graining is present. The reason behind this is that increasing q increases the numerical and statistical errors through the μ_k^q expression. As mentioned above, increasing error on the data makes it really difficult to get acceptable results from the MFSS.

As a result, in the range $0 \leqslant q \leqslant 1$ the critical point, W_c, and the critical exponent, ν, were found to be consistent with our results at fixed $\lambda = 0.1$ and based on the D_q and α_q exponents also with the high-precision result of Rodriguez *et al.* [15]. We observe the expected symmetry (14) for Δ_q and α_q, and our resulting MFEs fulfill these conditions in the range $0 \leqslant q \leqslant 1$.

Summarizing the results, it is possible to perform an MFSS at fixed $\ell = 1$ and achieve good agreement with previous high-precision results [15]. There are certainly numerical difficulties, however, that lead us to resort to the limited range of $0 \leqslant q \leqslant 1$ only, but with further averaging, the widening of this q range seems to be possible.

B. Numerical calculations for the 3D quantum percolation model using GMFEs

The main goal in the present study was to find the mobility edge and the critical exponent of the 3D quantum percolation model, and to investigate the multifractal properties of the critical wave functions. Since the Hamiltonian Eq. (2) is symmetric for $E \leftrightarrow -E$ exchange, the $E \geqslant 0$ interval is investigated only. We used the same numerics as in Sec III A 2. To avoid the frequent molecular states (see Sec. II A), and to cover the most interesting regions of the band, we chose the following energies: $E = 0.001$, 0.01, 0.1, 0.3, 0.7, 1.1, 1.5, 2.1, 3.1, 4.1. For averaging, we considered only one wave function per realization with the eigenvalue closest to the chosen energy E to avoid correlations. We only used an eigenfunction if its energy was in a $\Delta E = 0.01$ wide interval around E, except for $E = 0.001$ and 0.01, where $\Delta E = 0.00001$ and 0.001 were used.

Our ΔE energy intervals are so small that they completely exclude the effect of molecular states. We ran a test after the finite-size scaling was performed: Molecular states have a strict energy value, therefore at fixed system size L, disorder p, and energy E, we left out from our raw dataset all the wave functions with the same energy value (at most 2% of the original raw dataset). Note that these states are not necessarily molecular states; they can be regular ones too, having the same energy within numerical precision. We redid our whole finite-size scaling procedure (as described below), but this additional refinement had no effect on the results. This test ensures that we filtered out the molecular states very effectively, and if they were present in our raw dataset their effect would be negligible.

TABLE I. System sizes and number of samples of the simulation for the 3D quantum percolation model.

	Number of samples	
System size (L)	$p_c^Q < 0.41$	$p_c^Q > 0.41$
20	50000	50000
30	50000	50000
40	50000	50000
60	50000	25000
80	20000	10000
100	10000	5000
120	5000	
140	4000	

At every energy we searched for the critical point p_c^Q. From the approximately $\Delta p = 0.01$ wide neighborhood around p_c^Q we picked about 20 values of p. For higher p_c^Q values at fixed system size, L, there are more sites in the giant cluster, thus the Hamiltonian matrix is larger, and it takes more time to find the closest eigenvalue to the given energy. On the other hand, R_q and S_q are calculated from more data, thus they are more precise. Considering these arguments, we investigated system sizes and the number of samples listed in Table I. Altogether, 45 045 000 wave functions were calculated.

The method we used here has been described in Sec III A 2. We experienced that for typical averaging, finite-size scaling sometimes had difficulty converging, therefore we used the ensemble-averaged exponents $D_q^{\rm ens}$ and $\alpha_q^{\rm ens}$ only. The typical behavior of these exponents is presented in Fig. 4; note that curves do not have a common crossing point due to the $1/\ln L$ term in Eq. (29).

The MFSS at fixed $\ell = 1$ for the range $0 \leqslant q \leqslant 1$ provided critical points, critical exponents, and MFEs for every q value at every chosen energy, E. For fixed energy the critical points and critical exponents should be q-independent, which can be fulfilled within the 95% confidence level; see Fig. 5.

The critical point, p_c^Q, shifts in most cases, but the shift is within the 95% confidence band. An interesting feature is that p_c^Q obtained from α_q for $q \leqslant 0.5$ and $q \geqslant 0.5$ shifts in the opposite direction. For $\alpha_{0.4}$ and $\alpha_{0.6}$, the MFSS mostly did not converge since $\alpha_{0.5} = d$, and close to the $q = 0.5$ point, $\tilde{\alpha}$ curves have similar steepness close to the critical point, therefore it is numerically hard to determine a well-defined crossing point after scaling out the $\ln L$ shift. Therefore, these data are not presented in Fig. 5.

For $E = 0.001$ and 0.01, the MFSS showed severe convergence troubles, and even if it did converge, it provided fit parameters with very large error. The reason behind this behavior is presumably the close vicinity of the pseudogap at $E = 0$ in the DOS, and it is very hard even to find eigenvalues close enough to the desired energies $E = 0.001$ or 0.01. Another difficulty in this case is that the mobility edge becomes anomalous approaching $E = 0$; see Fig. 6(a). Therefore, only a narrow energy band is permitted for averaging around $E = 0.001$ or 0.01, which decreases further the possible number of eigenstates. For these reasons, parameters coming from MFSS at $E = 0.001$ and 0.01 were only used to plot the mobility edge; these two points are denoted with empty squares in Fig. 6(a).

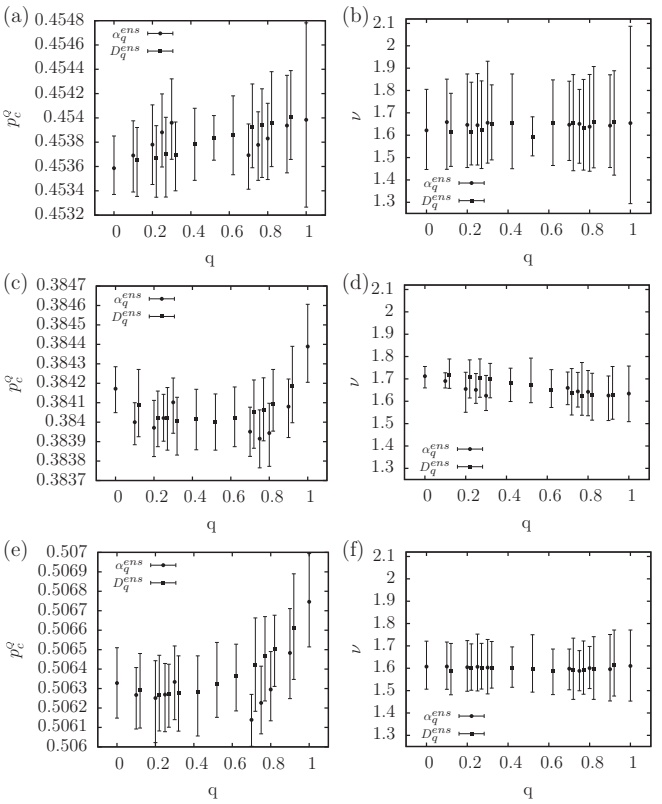

FIG. 5. Critical point (left column) and critical exponent (right column) of the 3D quantum percolation model at (a) and (b) $E = 0.1$, (c) and (d) $E = 0.7$, and (e) and (f) $E = 3.1$. Error bars represent 95% confidence levels.

At fixed energy we picked one q point that represents well the results for that energy; see Table II. The p_c^Q values are leading to a mobility edge; see Fig. 6(a). The values of ν are independent and should not depend on the energy. Thus they can be averaged, providing a more precise critical

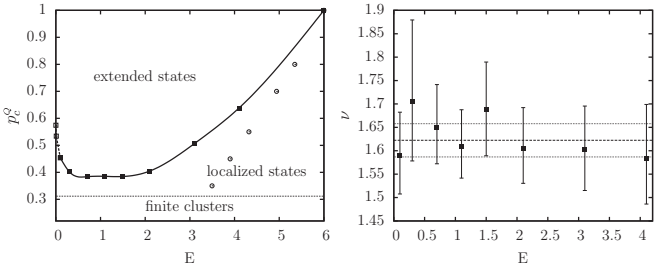

FIG. 6. (a) Mobility edge for the 3D quantum percolation model; the dotted line denotes the classical percolation threshold, $p_c^C = 0.3116 \pm 0.0002$ [3]. Circles are approximate values of the bandwidth; beyond them only the Lifshitz tail is present. Squares are results from MFSS, and the line is a spline to guide the eye. Empty squares and dashed lines are for approximate data obtained from MFSS at $E = 0.001$ and 0.01. (b) Critical exponent for the 3D quantum percolation model. Error bars are for the 95% confidence band. The dashed line is the average, and dotted lines note the 95% confidence band around the average. The resulting critical exponent is $\nu = 1.622$ (1.587, . . . ,1.658).

TABLE II. Resulting data along the mobility edge. These q values were chosen to compute ν and obtain the mobility edge.

E	MFE	p_c^Q	ν	NDF	χ^2	$L_{\min}$	$n_{\rm rel}$	n_ρ
0.1	$D_{0.5} = 2.421$ (2.416, ...,2.426)	0.45384 (0.45365, ...,0.45402)	1.591 1.508, ...,1.682	136	113	20	3	1
0.3	$D_{0.5} = 2.397$ (2.393, ...,2.402)	0.40241 (0.40228, ...,0.40257)	1.705 1.578, ...,1.879	157	123	20	3	1
0.7	$D_{0.6} = 2.271$ (2.265, ...,2.278)	0.38402 (0.38387, ...,0.38418)	1.645 1.572, ...,1.741	181	150	20	4	1
1.1	$D_{0.6} = 2.262$ (2.257, ...,2.268)	0.38518 (0.38504, ...,0.38531)	1.609 1.542, ...,1.688	243	155	20	3	1
1.5	$D_{0.8} = 2.027$ (2.020, ...,2.035)	0.38459 (0.38443, ...,0.38476)	1.688 1.589, ...,1.789	144	154	20	3	2
2.1	$D_{0.5} = 2.439$ (2.431, ...,2.448)	0.40466 (0.40443, ...,0.40492)	1.606 1.530, ...,1.692	127	116	40	2	2
3.1	$D_{0.4} = 2.542$ (2.538, ...,2.546)	0.50628 (0.50606, ...,0.50647)	1.603 1.515, ...,1.695	138	113	20	3	1
4.1	$\alpha_{0.9} = 2.108$ (2.101, ...,2.114)	0.63827 (0.63806, ...,0.63845)	1.584 1.486, ...,1.699	128	113	20	3	1

exponent $\nu = 1.622$ (1.587, ...,1.658); see Fig. 6(b). To derive the average, the data points were weighted by their inverse variance; the error bar is twice the standard deviation of the mean, which is about the 95% confidence band for a Gaussian.

In the literature, there are previous works showing a mobility edge [3,6,8,9,22]; see Fig. 7. The shapes of these curves are very similar: a steep decrease around $E = 0$, then a plateau resulting in a global quantum percolation threshold for the system, and finally an increasing behavior with growing energy. The curves are in good qualitative agreement with each other, and beyond $E = 3$ quantitative agreement is also present. Curves of Soukoulis [9] and Schubert [6] have jumps at $E = 1$ and $E = \sqrt{2}$ (only Ref. [6]) due most likely to the most frequent molecular states. Our curve is in very good agreement with the recent result of Travenec [22] obtained by transfer-matrix methods; the curves are almost covering each other. His critical exponent is also in good agreement with ours; see Table III.

At low p values the bandwidth is small, but increasing p results in a wider band. In the Lifshitz tail, only localized states are present, therefore the mobility edge curve should be above the curve of the bandwidth. As a result, the mobility edge curve increases at high energies in Fig. 6(a). Reaching the edge of the band, $E \to 6$, the mobility edges drawn from the data points of different authors seem to converge to 1. Therefore, we put a point in the top-right corner of Fig. 7; however, at $p = 1$ the sample is a perfect crystal, and wave functions are completely extended Bloch functions over the complete band.

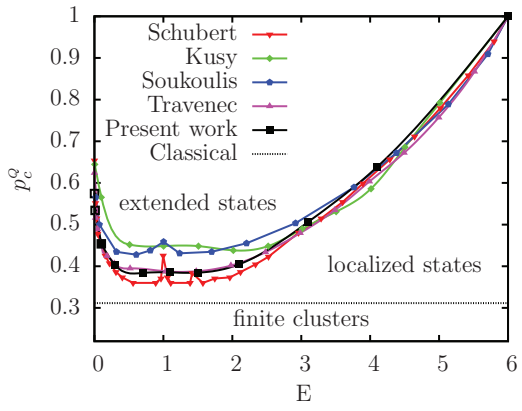

FIG. 7. (Color online) Mobility edge of the 3D quantum percolation model in the literature [3,6,8,9,22].

Exactly at the center of the band, $E = 0$, on the other hand, extremely localized molecular states disturb the picture. In addition, close to the band center a pseudogap forms in the DOS (see Fig. 1), therefore this regime is quite hard to investigate numerically. Even though the localized molecular states at $E = 0$ belong to the point spectrum, it is still not clear what the $E \to 0$ limit of the mobility edge is describing the continuous spectrum. The following question arises: Does the very steep increase of the mobility edge approaching $E = 0$ result in a $p_c^Q(E \to 0) \to 1$, or is the limit lower than 1? Based on the arguments in Sec. II A, our guess is that at any finite disorder, $p < 1$, there are localized states near $E = 0$, resulting in a limit of unity for the mobility edge, $p_c^Q(E \to 0) = 1$.

Some values of the critical exponent can also be found in the literature. In Table III, we collected these values ranging from 1.2 to 1.95. Because of the more limited computational efforts, previous works used much smaller system sizes compared to our possibilities, leading to much bigger finite-size effects, affecting their FSS. Conductivity or transfer matrix methods are used to overestimate, while level statistics and Green-function techniques are used to underestimate the critical exponent, ν. Our critical exponent is practically in the center of the interval of the previous results $1.2 \leqslant \nu \leqslant 1.95$. Our exponent, $\nu = 1.622$ (1.587, ...,1.658), is in very good agreement with the most recent study of Travenec [22], similarly to the mobility edge. Furthermore, the critical exponent is within the confidence band with our previous result for the Anderson model at fixed $\ell = 1$ obtained from $D_{0.6}^{\rm ens}$ [$\nu = 1.617$ (1.485, ...,1.783)] or at fixed $\lambda = 0.1$ obtained from $\alpha_{0.6}^{\rm ens}$ [$\nu = 1.598$ (1.576, ...,1.616)] even further with the high-precision value [$\nu = 1.590$ (1.579, ...,1.602)] of Rodriguez *et al.* [15], however our result seems to be a bit higher. Based on these facts, our work provides further evidence for previous conjectures and statements saying that the Anderson model and the 3D quantum percolation model belong to the same universality class.

IV. ANALYSIS OF MFEs OF THE 3D QUANTUM PERCOLATION METHOD

MFSS provided us the points of the $D_q(E)$ and $\alpha_q(E)$ surface at the investigated energies and q values. By inversion of the mobility edge curve, $p_c^Q(E)$, one can derive the MFEs as a function of p_c^Q and of q; see Fig. 8. Since $D_0 = d$, at small q values, i.e., $q \to 0$, the results for D_q are p_c^Q-independent, but for larger values of q the D_q starts to shift down with decreasing p_c^Q, which shows up in the lower right corner of Fig. 8(a).

TABLE III. Critical exponent of the 3D quantum percolation model in the literature.

Author	Year	ν	Method	System size
Root-Bauer-Skinner [26]	1988	1.8 ± 0.11	conductivity	$L = 3$–9
Koslowski–von Niessen [27]	1991	1.95 ± 0.12	conductivity	$L = 6$–9
Berkovits-Avishai [28]	1996	1.35 ± 0.1	level statistics	$L = 7$–15
Kusy *et al.* [8]	1997	1.2 ± 0.2	Green function	$L = 4$–8
Kaneko-Ohtsuki [29]	1999	1.46 ± 0.09	level statistics	$L = 12$–21
Travenec [22]	2008	1.6 ± 0.1	conductivity	$L = 14$–20
Present work	2014	1.622 ± 0.035	multifractality	$L = 20$–140

In the lower regime of Fig. 8(c) this shift is visibly significant. The same phenomenon can be detected for α_q. This suggests that D_q and α_q seem not to behave as universal quantities.

At relatively larger values of p_c^Q, D_q and α_q fulfill the symmetry relation (14); see Fig. 9(a), 9(b), 9(e), and 9(f). However, at the bottom of the mobility edge, where p_c^Q is smaller, meaning that the lattice is more diluted or more irregular, deviations from the symmetry law seem to be prominent. The D_q and α_q values remain the same at small q, i.e., when $q \to 0$, but they drop down as q increases. This leads to the conclusion that the symmetry relation, Eq. (14), is violated in this regime; see, for example, Figs. 9(c) and 9(d).

The nonuniversality of D_q and α_q would automatically imply the nonuniversality of τ_q as well. On the other hand, with a Legendre transform for τ_q, $f(\alpha)$ can be obtained, describing the scaling of the probability distribution of the wave-function amplitudes. This distribution should be universal, therefore $f(\alpha)$ should be universal, too. Using Eqs. (13) and (8), it immediately follows that

$$f(\alpha_q) = q\alpha_q - D_q(q-1). \tag{30}$$

From the α_q and D_q exponents presented in Figs. 8(a) and 8(b), we computed the $f(\alpha)$ curve, which is depicted in Fig. 10. The values from different regimes of the mobility edge seem to form a unique curve, but this is mostly due to the scale

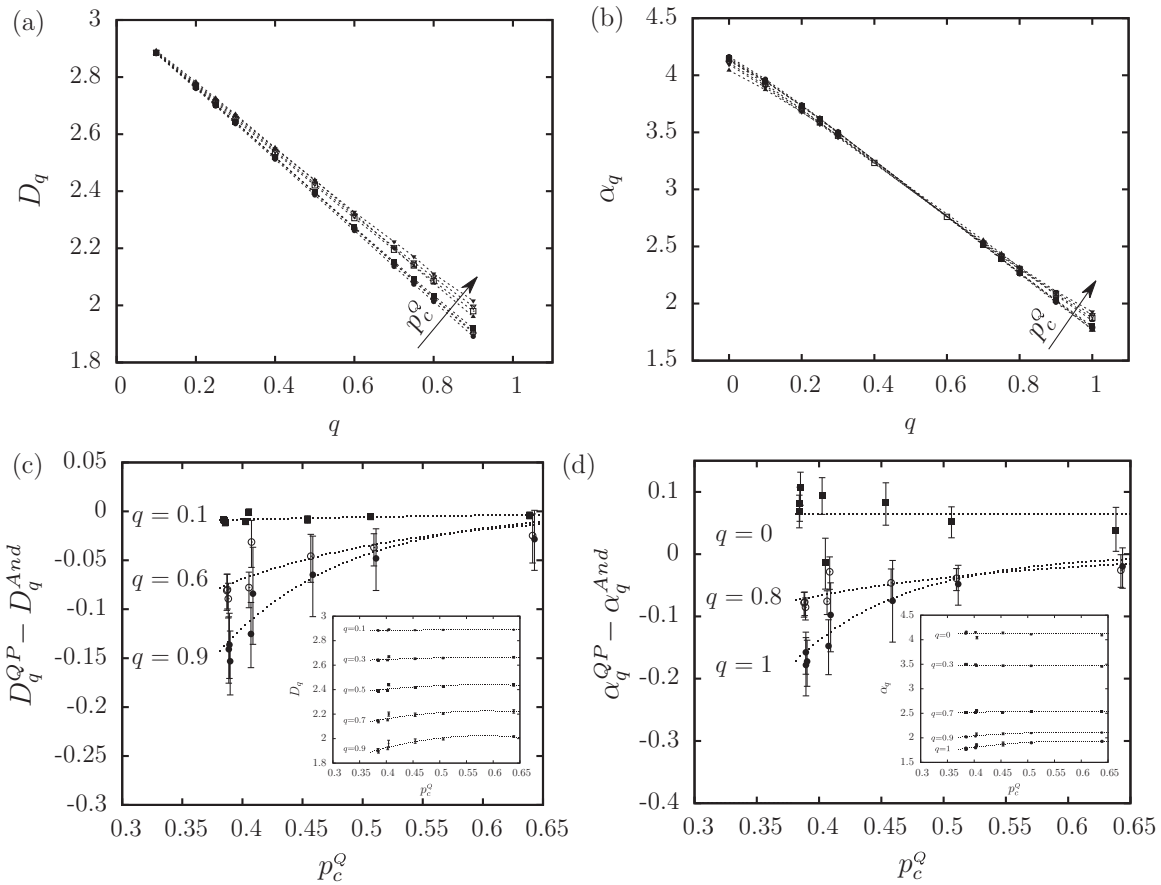

FIG. 8. First row: (a) D_q, (b) α_q as a function of q at different energies, E. Second row: GMFEs shifted by their value for the Anderson model, (a) $D_q^{\mathrm{QP}} - D_q^{\mathrm{And}}$ and (b) $\alpha_q^{\mathrm{QP}} - \alpha_q^{\mathrm{And}}$, as a function of p_c^Q at different q values. Dotted lines are guides for the eye, error bars represent a 95% confidence band on (c) and (d). Insets are the same, but without the shift.

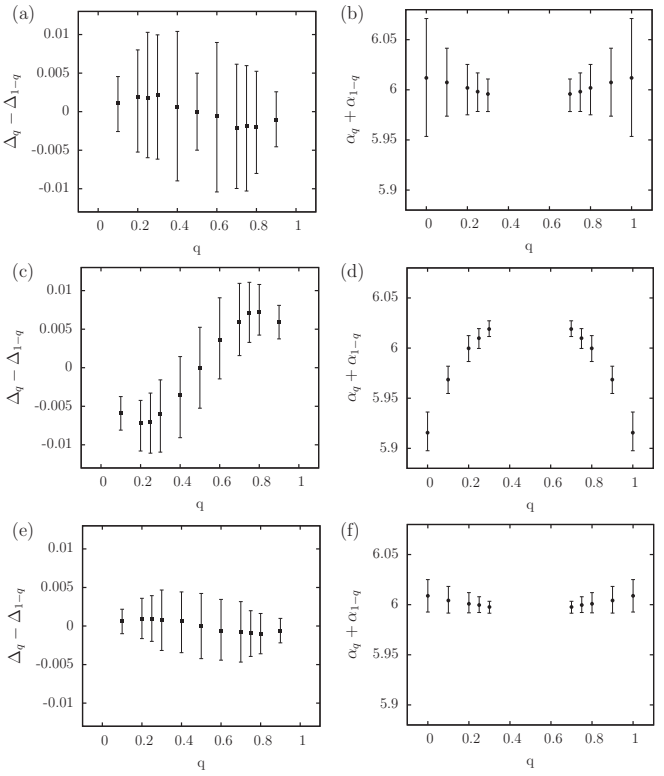

FIG. 9. Symmetry relation of Δ_q (left column) and α_q (right column) of the 3D quantum percolation model at (a) and (b) $E = 0.1$, (c) and (d) $E = 0.7$ (at the bottom of the mobility edge), and (e) and (f) $E = 3.1$. Error bars are 95% confidence levels. Points are naturally symmetric (antisymmetric) for $q = 0.5$ for α_q (Δ_q) because of the addition (subtraction) of terms corresponding to q and $1 - q$.

on the axis. The upper inset of Fig. 10 shows significant differences between data points at different energies. The approximate shape of the curve is a parabola, however a quartic curve fits the data points slightly better. According to Eq. (30), $q = 1$ corresponds to the fixed point of the $f(\alpha)$ function, $f(\alpha_1) = \alpha_1$. For different values of p_c^Q, the exponent α_1 is not unique, leading to a linear regime of the $f(\alpha)$ function; see the lower inset of Fig. 10. This makes the whole Legendre transformation difficult, since it needs strict convexity. Conversely, an $f(\alpha)$ that is not strictly convex would lead to ill-defined τ_q, D_q, and α_q, as in our case, which contradicts universality again. A possible resolution for this contradiction could be that our result for the MFEs is just simply not complete; perhaps a p-dependent phenomenon has not been taken into account affecting the results. Since the problem appeared at the bottom of the mobility edge, closest to the classical percolation threshold, one possible candidate for such a phenomenon is the existence of an additional length scale, namely the correlation length of the classical percolation. To test it, we added this length scale to the fitting function leading to a three-variable function with the number of fit parameters $\sim n_{\text{rel}}^3$, but we could not fit so many parameters in our dataset. There is only a small difference between the values of the MFEs for the quantum percolation model and those for the Anderson model, see Fig. 8, and the symmetry relation (14) is almost valid within the error bar at the bottom of the mobility

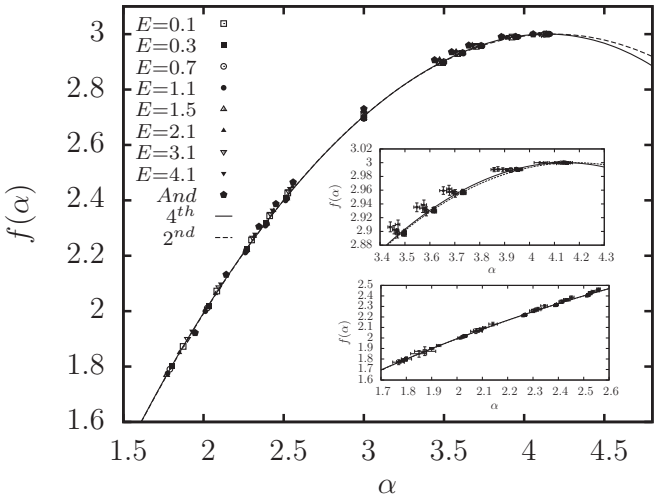

FIG. 10. $f(\alpha)$ obtained from D_q and α_q computed at different energies, meaning different p_c^Q. Pentagons are the results for the Anderson model, the solid line is a fourth-order polynomial, and the dashed line is a second-order polynomial. Insets are magnified parts of the curve.

edge, too; see Fig. 9. Therefore, another explanation would be that somehow we underestimated the error bars of the MFEs. In the $p \to 1$ limit, our exponents seem to be close to their value for the Anderson model, which, together with our former claim in Sec. III B about their matching universality class, corroborates this possibility further. We believe that there is a unique and universal D_q, α_q, and $f(\alpha)$ curve for the quantum percolation method, and it is identical to the one for the Anderson model, which fulfills the symmetry relation (14).

In conclusion, the present coherent set of data with a coherent technology in deriving critical exponents fulfills our expectations for larger values of $p_c^Q \geqslant 0.5$, but unfortunately unexpected deviations occur for lower values, i.e., $p_c^Q \leqslant 0.5$.

V. SUMMARY

In the present work, we have numerically investigated the quantum percolation model in three dimensions. We developed the MFSS method by Rodriguez *et al.* [15] in order to use it for irregular lattices, or even for graphs in the future. First we tested our method on the well-known Anderson model, however certain numerical issues forced us to restrict our analysis to the interval $0 \leqslant q \leqslant 1$. We found q-independent results in good agreement with the previous high-precision values of Ref. [15]. Then we used our method for the quantum percolation model, where we found q-independent results again. We numerically determined the mobility edge of the system, confirming previous calculations. We also gave an explanation for the behavior of the mobility edge near $E = 0$ and at high energy. For the critical exponent, we got energy-independent values within a 95% confidence level. The average of these values is the same as the one for the critical exponent for the Anderson model, implying that these models belong to the same universality class. We also determined the MFEs D_q and α_q along the mobility edge, and for larger values of p_c^Q we found no significant difference from the Anderson model,

confirming the statement of the same universality class further. In this regime, the symmetry relation (14) is fulfilled. On the other hand, in the case of lower p_c^Q regime the exponents started to deviate violating universality and (14), probably caused by some unexpected p-dependent phenomenon. This behavior deserves further attention.

ACKNOWLEDGMENTS

The authors are indebted to A. Stathopoulos for his help setting up the numerical method. Financial support from OTKA under Grant No. K108676, the Alexander von Humboldt Foundation, are gratefully acknowledged.

[1] P. W. Anderson, Phys. Rev. **109**, 1492 (1958).
[2] F. Evers and A. D. Mirlin, Rev. Mod. Phys. **80**, 1355 (2008), and references therein.
[3] D. Stauffert and J. G. Zabolitzky, J. Phys. A **19**, 3705 (1986).
[4] K. Christensen and N. R. Moloney, *Complexity and Criticality* (Imperial College Press, London, 2005).
[5] M. E. J. Newman and R. M. Ziff, Phys. Rev. Lett. **85**, 4104 (2000).
[6] G. Schubert and H. Fehske, *Quantum and Semi-Classical Percolation and Breakdown in Disordered Solids*, Lecture Notes in Physics, Vol. 762 (Springer, Berlin, 2009), pp. 135–162.
[7] S. Kirkpatrick and T. P. Eggarter, Phys. Rev. B **6**, 3598 (1972).
[8] A. Kusy, A. W. Stadler, G. Haldas, and R. Sikora, Physica A **241**, 403 (1997).
[9] C. M. Soukoulis, Q. Li, and G. S. Grest, Phys. Rev. B **45**, 7724 (1992).
[10] J. Hoshen and R. Kopelman, Phys. Rev. B **14**, 3438 (1976).
[11] A. Stathopoulos and J. R. McCombs, ACM Trans. Math. Software **37**, 21 (2010).
[12] O. Schenk, M. Bollhöfer, and R. A. Römer, SIAM Rev. **50**, 91 (2008).
[13] C. Bordenave, A. Sen, and B. Virag, arXiv:1308.3755.
[14] G. G. Naumis, Ch. Wang, and R. A. Barrio, Phys. Rev. B **65**, 134203 (2002).
[15] A. Rodriguez, L. J. Vasquez, K. Slevin, and R. A. Römer, Phys. Rev. B **84**, 134209 (2011).
[16] M. Janssen, *Fluctuations and Localization in Mesoscopic Electron Systems*, World Scientific Lecture Notes in Physics Vol. 64 (World Scientific, Singapore, 2001); Phys. Rep. **295**, 1 (1998).
[17] E. Cuevas and V. E. Kravtsov, Phys. Rev. B **76**, 235119 (2007).
[18] A. D. Mirlin, Y. V. Fyodorov, A. Mildenberger, and F. Evers, Phys. Rev. Lett. **97**, 046803 (2006).
[19] A. Mildenberger and F. Evers, Phys. Rev. B **75**, 041303(R) (2007).
[20] F. Evers, A. Mildenberger, and A. D. Mirlin, Phys. Status Solidi B **245**, 284 (2008); Phys. Rev. Lett. **101**, 116803 (2008).
[21] L. J. Vasquez, A. Rodriguez, and R. A. Römer, Phys. Rev. B **78**, 195106 (2008); A. Rodriguez, L. J. Vasquez, and R. A. Römer, *ibid.* **78**, 195107 (2008); Phys. Rev. Lett. **102**, 106406 (2009).
[22] I. Travenec, Int. J. Mod. Phys. B **22**, 5217 (2008).
[23] A. R. Subramaniam, I. A. Gruzberg, A. W. W. Ludwig, F. Evers, A. Mildenberger, and A. D. Mirlin, Phys. Rev. Lett. **96**, 126802 (2006).
[24] S. Faez, A. Strybulevych, J. H. Page, A. Lagendijk, and B. A. van Tiggelen, Phys. Rev. Lett. **103**, 155703 (2009).
[25] C. Monthus and Th. Garel, J. Stat. Mech. (2011) P05005; see also C. Monthus, B. Berche, and Ch. Chatelain, *ibid.* (2009) P12002.
[26] L. J. Root, J. D. Bauer, and J. L. Skinner, Phys. Rev. B **37**, 5518 (1988).
[27] Th. Koslowski and W. von Niessen, Phys. Rev. B **44**, 9926 (1991).
[28] R. Berkovits and Y. Avishai, Phys. Rev. B **53**, R16125(R) (1996).
[29] A. Kaneko and T. Ohtsuki, J. Phys. Soc. Jpn. **68**, 1488 (1999).